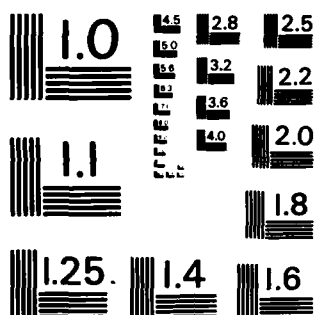


AD-A148 537	AN EFFICIENT NUMERICAL SOLUTION TECHNIQUE FOR WAVE PROPAGATION IN HORIZON. (U) SACLANT ASW RESEARCH CENTRE LA SPEZIA (ITALY) H SCHMIDT ET AL. 01 AUG 84	1/1
UNCLASSIFIED	SACLANTCEN-SM-173	F/G 12/1 NL

[illegible]



AD-A148 537

DTIC FILE COPY

SACLANT ASW  
RESEARCH CENTRE  
MEMORANDUM



SACLANTCEN Memorandum SM -173

AN EFFICIENT NUMERICAL SOLUTION TECHNIQUE  
FOR WAVE PROPAGATION  
IN HORIZONTALLY STRATIFIED OCEAN ENVIRONMENTS

by

Henrik SCHMIDT  
Finn B. JENSEN

DTIC  
ELECTE  
DEC 14 1984

1 AUGUST 1984

This document has been approved  
for public release and sale; its  
distribution is unlimited.

NORTH  
ATLANTIC  
TREATY  
ORGANIZATION

SACLANTCEN  
LA SPEZIA, ITALY

This document is unclassified. The information it contains is published subject to the conditions of the legend printed on the inside cover. Short quotations from it may be made in other publications if credit is given to the author(s). Except for working copies for research purposes or for use in official NATO publications, reproduction requires the authorization of the Director of SACLANTCEN.

This document is released to a NATO Government at the direction of the SACLANTCEN subject to the following conditions:

1. The recipient NATO Government agrees to use its best endeavours to ensure that the information herein disclosed, whether or not it bears a security classification, is not dealt with in any manner (a) contrary to the intent of the provisions of the Charter of the Centre, or (b) prejudicial to the rights of the owner thereof to obtain patent, copyright, or other like statutory protection therefor.

2. If the technical information was originally released to the Centre by a NATO Government subject to restrictions clearly marked on this document the recipient NATO Government agrees to use its best endeavours to abide by the terms of the restrictions so imposed by the releasing Government.

Published by



SACLANTCEN MEMORANDUM SM-173

ORGANIZATION  
Research Centre  
Piazzale Michelangelo 400,  
10126 Turin (SP), Italy.

0187 540111  
09 187 540111  
1148 SACENT I

AN EFFICIENT NUMERICAL SOLUTION TECHNIQUE  
FOR WAVE PROPAGATION  
IN HORIZONTALLY STRATIFIED OCEAN ENVIRONMENTS

by  
Henrik Schmidt  
Finn B. Jensen

1 August 1984

SACLANT ASW Research Centre  
Viale San Bartolomeo 400,  
I-19026 San Bartolomeo (SP), Italy.

**AN EFFICIENT NUMERICAL SOLUTION TECHNIQUE  
FOR WAVE PROPAGATION  
IN HORIZONTALLY STRATIFIED OCEAN ENVIRONMENTS**

by  
**Henrik Schmidt  
Finn B. Jensen**

**1 August 1984**

**AN EFFICIENT NUMERICAL SOLUTION TECHNIQUE  
FOR WAVE PROPAGATION  
IN HORIZONTALLY STRATIFIED OCEAN ENVIRONMENTS**

by  
**Henrik Schmidt  
Finn B. Jensen**

**1 August 1984**

**AN EFFICIENT NUMERICAL SOLUTION TECHNIQUE  
FOR WAVE PROPAGATION  
IN HORIZONTALLY STRATIFIED OCEAN ENVIRONMENTS**

by  
**Henrik Schmidt  
Finn B. Jensen**

**1 August 1984**

**AN EFFICIENT NUMERICAL SOLUTION TECHNIQUE  
FOR WAVE PROPAGATION  
IN HORIZONTALLY STRATIFIED OCEAN ENVIRONMENTS**

by  
**Henrik Schmidt  
Finn B. Jensen**

**1 August 1984**

D. F. Hocking.

[illegible]

TABLE OF CONTENTS

	<u>Pages</u>
ABSTRACT	1
INTRODUCTION	1
1 DERIVATION OF FIELD EQUATIONS	2
2 NUMERICAL SOLUTION TECHNIQUE	7
3 COMPUTATIONAL EXAMPLES	13
3.1 Sea-surface interference effects	13
3.2 Propagation in a shallow-water duct	15
3.3 Beam reflection at a water/bottom interface	19
SUMMARY AND CONCLUSIONS	23
APPENDIX A - NUMERICAL STABILITY	25
REFERENCES	27

List of Figures

1. Horizontally stratified medium.	3
2. Mapping between local and global systems of equations.	9
3. Lloyd-mirror beams at the sea surface (a), and associated angular spectrum (b).	14
4. Horizontal wavenumber spectrum for shallow water case at 30 Hz (a), and associated transmission loss curves (b).	16
5. Horizontal wavenumber spectrum for shallow water case at 5 Hz (a), and associated transmission loss curves (b).	18
6. Reflection and transmission of narrow beam of sound ( $D=2.5\lambda$ ) at water/bottom interface. The critical angle is $30^\circ$ and there is no attenuation in the bottom.	21
7. Angular spectra of incident beams of different half-power widths (a), and reflectivity characteristics at water/bottom interface (b).	22
8. Deviation from Snell's law for reflection and transmission of narrow beam of sound at water/bottom interface.	24
A.1 Mapping ensuring numerical stability in evanescent case.	26

# AN EFFICIENT NUMERICAL SOLUTION TECHNIQUE FOR WAVE PROPAGATION IN HORIZONTALLY STRATIFIED OCEAN ENVIRONMENTS

by

Henrik Schmidt and Finn B. Jensen

## ABSTRACT

A new solution technique for wave propagation in horizontally stratified viscoelastic media is presented. The model provides a full-wave solution for the field generated by a single source, as well as for that generated by a vertical source array. It allows the spatial distribution of the acoustic field to be evaluated at least one order of magnitude faster than with existing models based on the Thomson-Haskell solution technique. Computational examples demonstrate the model's versatility in providing exact solutions to a wide range of guided and non-guided propagation problems in underwater acoustics.

## INTRODUCTION

A numerical model providing a full-wave solution to propagation problems in horizontally stratified fluid/solid environments is presented. During the last decade a number of similar models have been developed, known in underwater acoustics as Fast Field Programs <1-3> and in seismology as full wave field response models <4>. These models are, however, in general based on the Thomson-Haskell matrix method, which allows for field calculations for only one source/receiver combination at a time. Hence calculations of the field as a function of depth and of fields produced by vertical source arrays need several separate runs, with the calculation time being proportional to the number of sources and receivers.

In this model a more direct approach is taken. The field is considered as a superposition of two fields: one produced by the sources in the absence of boundaries, and an unknown field satisfying the homogeneous wave equation. The unknown field is then determined from the boundary conditions to be satisfied at each interface. This approach is equivalent to the technique used by Ewing et al <5> to derive analytic solutions, although not in closed form, for special cases with only a few layers. The model described here is in fact just a general numerical implementation of their approach, but compared with the Thomson-Haskell technique there are a number of important advantages. First there are no restrictions on the number of sources, as the fields produced by more sources within a layer are simply superimposed. Second, any number of receiver depths can be treated with one solution, since the unknown field is found in all layers simultaneously. Thus the spatial distribution of the field produced by a

single source or by a beam-generating vertical array can be determined in a computationally efficient manner. Third, even for only one source/receiver combination, this solution technique as implemented here yields a code that is an order of magnitude faster than existing models using the Thomson-Haskell technique. This is partly due to the fact that the Thomson-Haskell technique requires additional specialized numerical effort in order to ensure stability in cases where evanescent waves are propagating in very thick layers. Such problems, by contrast, are removed automatically from this direct global solution technique by choosing a proper local coordinate system within each layer.

We describe the theoretical basis for wave propagation in stratified viscoelastic media in Sect. 1, following closely Ewing et al <5>. The numerical-solution technique particular to this model is described in Sect. 2, with details on the numerical stability being addressed in Appendix A. Section 3 is dedicated to computational examples for three important propagation problems in underwater acoustics: 1) Lloyd-mirror interference effects at the sea surface, 2) low-frequency propagation in a shallow-water duct, and 3) reflection of a narrow beam of sound at the sea floor. The paper ends with a summary and conclusions.

## 1 DERIVATION OF FIELD EQUATIONS

The representation of the field in terms of integral solutions closely follows the presentation given by Ewing et al <5> and thus only an outline is given here. The environment is assumed to be horizontally stratified and all layers, including the upper and lower half spaces, are considered to be isotropic and homogeneous viscoelastic continua with Lamé constants  $\lambda_n$  and  $\mu_n$  and density  $\rho_n$ . The subscript  $n$  refers to the layer number.

The field equations are here derived in cylindrical geometry. The derivation of the corresponding field representations in plane geometry is given elsewhere <6>.

A cylindrical coordinate system  $\{r, \theta, z\}$  is introduced, with the  $z$ -axis perpendicular to the interfaces and positive downwards, see Fig. 1. In the absence of body forces the equations of motion will be satisfied if the displacement components  $\{u, v, w\}$  in layer ' $n$ ' are expressed in terms of the scalar potentials  $\{\phi_n, \psi_n, \Lambda_n\}$  as

$$u(r, \theta, z) | _n = \frac{\partial \phi_n}{\partial r} + \frac{1}{r} \frac{\partial \psi_n}{\partial \theta} + \frac{\partial^2 \Lambda_n}{\partial r \partial z} \quad (\text{Eq. 1})$$

$$v(r, \theta, z) | _n = \frac{1}{r} \frac{\partial \phi_n}{\partial \theta} - \frac{\partial \psi_n}{\partial r} + \frac{1}{r} \frac{\partial^2 \Lambda_n}{\partial \theta \partial z} \quad (\text{Eq. 2})$$

$$w(r, \theta, z) | _n = \frac{\partial \phi_n}{\partial z} - \left( \frac{1}{r} \frac{\partial}{\partial r} r \frac{\partial}{\partial r} + \frac{1}{r^2} \frac{\partial^2}{\partial \theta^2} \right) \Lambda_n, \quad (\text{Eq. 3})$$



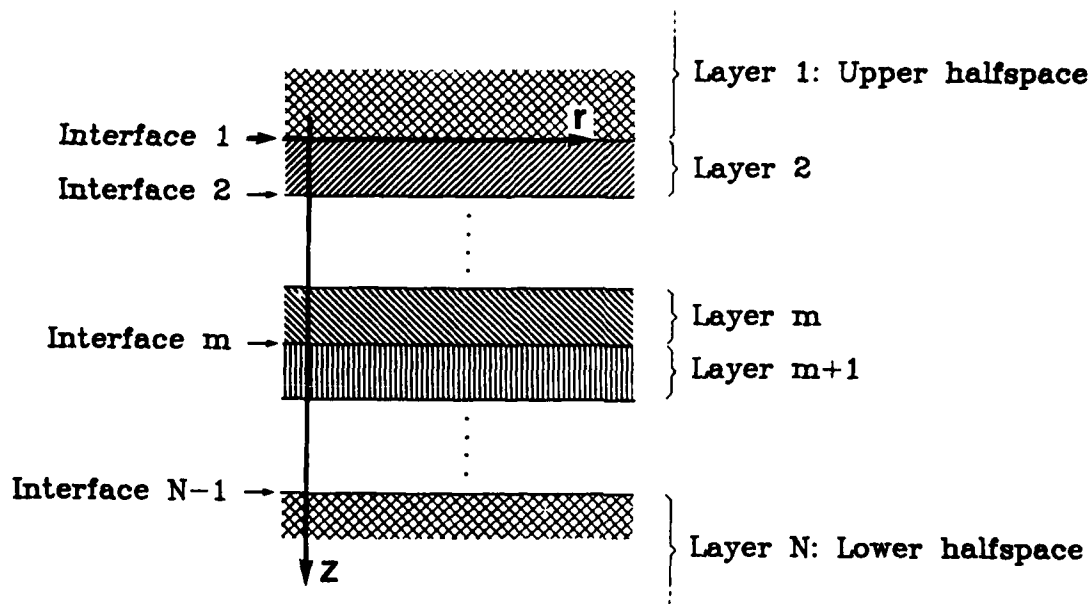


FIG. 1 HORIZONTALLY STRATIFIED MEDIUM.

where the potentials satisfy the wave equations

$$\left( \nabla^2 - \frac{1}{c_{cn}^2} \frac{\partial^2}{\partial t^2} \right) \phi_n = 0 \quad (\text{Eq. 4})$$

$$\left( \nabla^2 - \frac{1}{c_{sn}^2} \frac{\partial^2}{\partial t^2} \right) \{ \psi_n, \chi_n \} = 0. \quad (\text{Eq. 5})$$

Here  $c_{cn}$  and  $c_{sn}$  are the velocities of compressional and shear waves respectively:

$$c_{cn} = \sqrt{\frac{\lambda_n + 2\mu_n}{\rho_n}} \quad (\text{Eq. 6})$$

$$c_{sn} = \sqrt{\frac{\mu_n}{\rho_n}}. \quad (\text{Eq. 7})$$

If the medium is a fluid,  $\mu_n$  vanishes, and only the potential  $\phi_n$  is present. This can however be considered as a special case of the general solid case, and only when necessary is it treated separately in the following.

The sources are assumed to be harmonic and vibrate with the common angular frequency  $\omega$ . In complex notation a time dependence of the form  $\exp(i\omega t)$  is assumed, a common factor that will be omitted in the following. The viscoelastic attenuation can be accounted for by letting the Lamé constants be complex. The wave equations, Eqs. 4 and 5, now take the form

$$(\nabla^2 + h_n^2) \phi_n = 0 \quad (\text{Eq. 8})$$

$$(\nabla^2 + k_n^2) \{\psi_n, \Lambda_n\} = 0, \quad (\text{Eq. 9})$$

where  $h_n$  and  $k_n$  are the wavenumbers for compressional and shear waves respectively:

$$h_n^2 = \left(\frac{\omega}{c_{cn}}\right)^2 = \frac{\omega^2 \rho_n}{\lambda_n + 2\mu_n} \quad (\text{Eq. 10})$$

$$k_n^2 = \left(\frac{\omega}{c_{sn}}\right)^2 = \frac{\omega^2 \rho_n}{\mu_n} \quad (\text{Eq. 11})$$

If only compressional sources placed on the axis  $r=0$  are allowed, the field will be axisymmetric with vanishing tangential displacements  $v(r,z)$ . The torsional potential  $\psi_n$  can then be excluded from the analysis.

By applying the Hankel transform to Eqs. 8 and 9 the following integral representations are obtained for the solutions <5>:

$$\phi_n(r,z) = \int_0^\infty [A_n^-(s)e^{-z\alpha_n(s)} + A_n^+(s)e^{z\alpha_n(s)}] s J_0(rs) ds \quad (\text{Eq. 12})$$

$$\Lambda_n(r,z) = \int_0^\infty [B_n^-(s)e^{-z\beta_n(s)} + B_n^+(s)e^{z\beta_n(s)}] J_0(rs) ds, \quad (\text{Eq. 13})$$

where  $A_n^-$ ,  $A_n^+$ ,  $B_n^-$  and  $B_n^+$  are arbitrary functions in the horizontal wave-number 's', and where

$$\alpha_n(s) = \sqrt{s^2 - h_n^2} \quad (\text{Eq. 14})$$

$$\beta_n(s) = \sqrt{s^2 - k_n^2}. \quad (\text{Eq. 15})$$

Note that Eqs. 12 and 13 are just decompositions of the total fields in up and downgoing conical waves integrated over all angles (wavenumbers).

Because of the attenuation and the choice of time factor, the imaginary parts of  $h_n$  and  $k_n$  are negative, and the complex  $s$ -plane is cut along branches going from  $h_n$  and  $k_n$  to  $-i\infty$  and from  $-h_n$  and  $-k_n$  to  $+i\infty$ .

Substituting Eqs. 12 and 13 into Eqs. 1 and 3 gives the following integral representations for the displacements:

$$u(r,z) \big|_n = \int_0^\infty \left\{ -s A_n^- e^{-z\alpha_n} - s A_n^+ e^{z\alpha_n} + \beta_n B_n^- e^{-z\beta_n} - \beta_n B_n^+ e^{z\beta_n} \right\} s J_1(rs) ds \quad (\text{Eq. 16})$$

$$w(r,z) \big|_n = \int_0^\infty \left\{ -\alpha_n A_n^- e^{-z\alpha_n} + \alpha_n A_n^+ e^{z\alpha_n} + s B_n^- e^{-z\beta_n} + s B_n^+ e^{z\beta_n} \right\} s J_0(rs) ds. \quad (\text{Eq. 17})$$

The stress components involved in the boundary conditions follow by Hooke's law:

$$\begin{aligned} \sigma_{zz}(r,z) \big|_n &= \lambda_n \nabla^2 \phi_n + 2\mu_n \frac{\partial w}{\partial z} \\ &= \mu_n \int_0^\infty \left\{ (2s^2 - k_n^2) (A_n^- e^{-z\alpha_n} + A_n^+ e^{z\alpha_n}) + 2s\beta_n (-B_n^- e^{-z\beta_n} + B_n^+ e^{z\beta_n}) \right\} s J_0(rs) ds, \quad (\text{Eq. 18}) \end{aligned}$$

$$\begin{aligned} \sigma_{rz}(r,z) \big|_n &= \mu_n \left( \frac{\partial u}{\partial z} + \frac{\partial w}{\partial r} \right) \\ &= \mu_n \int_0^\infty \left\{ 2s\alpha_n (A_n^- e^{-z\alpha_n} - A_n^+ e^{z\alpha_n}) - (2s^2 - k_n^2) (B_n^- e^{-z\beta_n} + B_n^+ e^{z\beta_n}) \right\} s J_1(rs) ds. \quad (\text{Eq. 19}) \end{aligned}$$

In the case of a fluid layer the displacements follow directly from Eqs. 16 and 17 by setting  $B_n^-$  and  $B_n^+$  to zero. The shear stress  $\sigma_{rz}$  vanishes, whereas Eq. 18 has to be replaced by

$$\sigma_{zz}(r,z) \big|_n = -\lambda_n h_n^2 \int_{-\infty}^{\infty} \{A_n^- e^{-z\alpha_n} + A_n^+ e^{z\alpha_n}\} sJ_0(rs) ds. \quad (\text{Eq. 20})$$

To obtain expressions for the total field in layer 'n', the field produced by the sources within the layer has to be added. Only compressional sources at  $r=0$  are considered and the field produced by each, in an infinite medium with the material properties of layer 'n', has the integral representation <5>:

$$\Phi_n^*(r,z) = \int_0^{\infty} \frac{e^{-|z-z_s|\alpha_n}}{\alpha_n} sJ_0(rs) ds, \quad (\text{Eq. 21})$$

$$\Lambda_n^*(r,z) \equiv 0, \quad (\text{Eq. 22})$$

where  $z_s$  is the source depth.

The corresponding displacements involved in the boundary conditions are again obtained from Eqs. 1 and 3 as:

$$u(r,z) \big|_n = - \int_0^{\infty} \frac{s e^{-|z-z_s|\alpha_n}}{\alpha_n} sJ_1(rs) ds \quad (\text{Eq. 23})$$

$$w(r,z) \big|_n = - \int_0^{\infty} \text{sign}(z-z_s) e^{-|z-z_s|\alpha_n} sJ_0(rs) ds, \quad (\text{Eq. 24})$$

while the stresses are given by Hooke's law:

$$\sigma_{zz}(r,z) \big|_n = \mu_n \int_0^{\infty} (2s^2 - k_n^2) \frac{e^{-|z-z_s|\alpha_n}}{\alpha_n} sJ_0(rs) ds \quad (\text{Eq. 25})$$

$$\sigma_{xz}(r,z) \big|_n = \mu_n \int_0^{\infty} 2s \text{sign}(z-z_s) e^{-|z-z_s|\alpha_n} sJ_1(rs) ds. \quad (\text{Eq. 26})$$

In the fluid case, Eq. 25 is replaced by

$$\sigma_{zz}(r,z) \big|_n = \lambda_n h_n^2 \int_0^{\infty} \frac{e^{-|z-z_s|\alpha_n}}{\alpha_n} sJ_0(rs) ds. \quad (\text{Eq. 27})$$

If more than one source is present in the layer, the kernels in Eqs. 23 to 27 are replaced by a sum over the number of sources.

The field at each interface now has two different integral representations, one from the layer above and one from the layer below. The boundary conditions have to be satisfied at all ranges  $r$ ; thus they have to be satisfied by the kernels in the integral representations as well, leading to a linear system of equations in the unknown arbitrary functions  $A^+$ ,  $A^-$ ,  $B^+$  and  $B^-$ . This system can of course be solved analytically, as done for special cases in <5>, but for a general multilayered environment a numerical solution is more convenient. This numerical solution and the subsequent evaluation of the integral transforms is treated in the next section.

## 2 NUMERICAL SOLUTION TECHNIQUE

The numerical solution is divided into two parts. First the unknown arbitrary functions are found at a discrete number of horizontal wavenumbers from the system of equations that expresses the boundary conditions to be satisfied. Secondly the field is found at selected depths by evaluation of the integral transforms. The first part is the most critical in relation to computation time, and this is the part where the present model differs in approach from earlier models of the same type. Most emphasis is therefore given to this part in the following.

The layers are numbered from 1 to  $N$  (Fig. 1) where the upper halfspace is number 1 and the lower halfspace is number  $N$ . If the kernels for the field parameters involved in the boundary conditions at interface ' $m$ ', and evaluated in layer ' $n$ ', are expressed in vector form as  $\{v\}_n^m$ , then the local system of equations to be satisfied at interface ' $m$ ' is

$$\{v\}_m^m = \{v\}_m^m + \{v\}_m^{*m} = \{v\}_{m+1}^m + \{v\}_{m+1}^{*m}, \quad (\text{Eq. 28})$$

where the asterisk denotes the source contribution. Here and in the following the subscript refers to the layer number and the superscript to the interface number. In the general solid/solid case, Eq. 28 expresses continuity of  $u$ ,  $w$ ,  $\sigma_{zz}$  and  $\sigma_{rz}$ . If one of the media is a fluid,  $w$ ,  $\sigma_{zz}$  and  $\sigma_{rz}$  has to be continuous, whereas the fluid/fluid case requires only continuity of  $w$  and  $\sigma_{zz}$ . Where one of the media is a vacuum the stresses  $\sigma_{zz}$  and  $\sigma_{rz}$  must vanish. The number of elements in the vectors  $\{v\}_n^m$  therefore vary from interface to interface.

The contributions from the unknown homogeneous solutions are now isolated on the left-hand side, and Eq. 28 can be rewritten as

$$[c]_m^m \{a\}_m - [c]_{m+1}^m \{a\}_{m+1} = \{v\}_{m+1}^{*m} - \{v\}_m^{*m}, \quad (\text{Eq. 29})$$

where  $[c]_m^n$  is a coefficient matrix and  $\{a\}_m$  is a vector including the

degrees of freedom for layer 'm', i.e. all or some of the arbitrary functions  $A_m^-$ ,  $A_m^+$ ,  $B_m^-$  and  $B_m^+$ .

To combine the N-1 local systems of equations (one for each interface) into one global system, the following unique mapping is introduced:

$$\{a\}_m = [S]_m \{A\} \quad (\text{Eq. 30})$$

$$\{V\} = \sum_{i=1}^{N-1} [T]^i \{v\}^i \quad (\text{Eq. 31})$$

Here  $\{A\}$  and  $\{V\}$  are global vectors containing all degrees of freedom and field parameters involved in the boundary conditions. The matrices  $[S]_m$  and  $[T]^i$  are extremely sparse, containing only zeroes and ones. These matrices are very similar to the topology matrices known from the finite-element technique, and as is the case there, they are never set up in the actual computer code, but replaced by a set of pointers <7>.

Insertion of the mappings of Eqs. 30 and 31 into Eq. 29 yields the following global system of equations

$$[C]\{A\} = \{V\}^* \quad (\text{Eq. 32})$$

where the coefficient matrix is

$$[C] = \sum_{i=1}^{N-1} ([T]^i [c]_i^i [S]_i - [T]^i [c]_{i+1}^i [S]_{i+1}^i). \quad (\text{Eq. 33})$$

The right-hand side due to the source contributions is

$$\{V\}^* = \sum_{i=1}^{N-1} [T]^i (\{v\}_{i+1}^* - \{v\}_i^*) \quad (\text{Eq. 34})$$

As the mappings of Eqs. 30 and 31 are unique, the summations and the matrix multiplications in Eqs. 33 and 34 never need be performed, but can be replaced by a unique set of pointers connecting the elements of the global system with those of the similar local systems, as illustrated in Fig. 2.

The pointers defined by the mappings of Eqs. 30, 31, 33 and 34 are dependent only on the environment and can thus be determined a priori. The calculations needed at each horizontal wavenumber are then delimited to the creation of the local coefficient matrices and right-hand sides, and to the solution of Eq. 32. Then the kernels in Eqs. 16 to 20 and 23 to 27 can be determined for any number of depths.

Local system:

$$[c]_m^m \{a\}_m - [c]_{m+1}^m \{a\}_{m+1} = \{\dot{v}\}_{m+1}^m - \{\dot{v}\}_m^m$$

Global system:

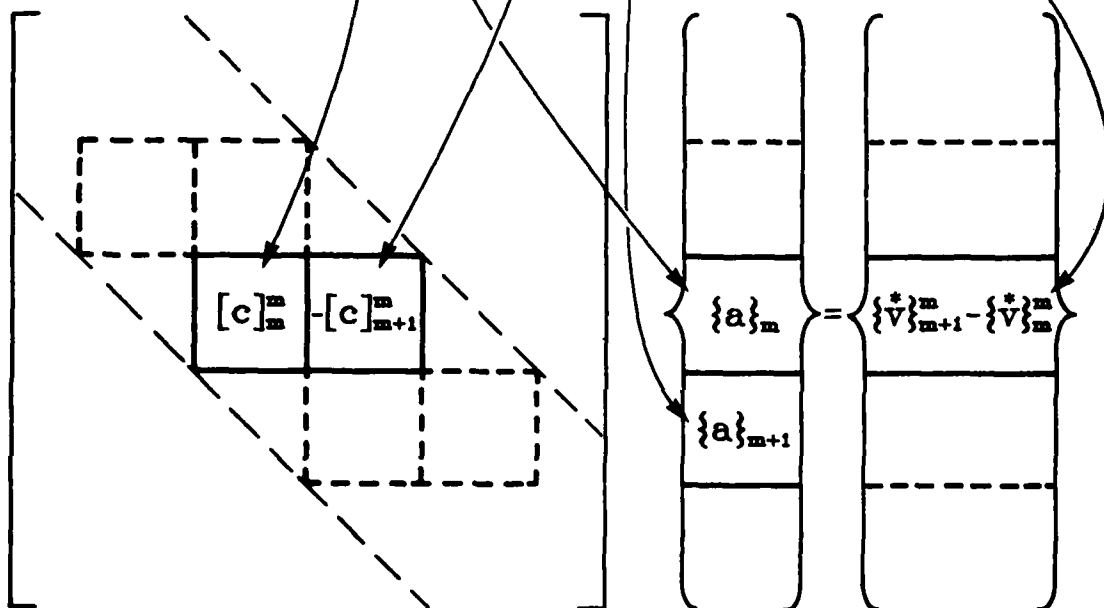


FIG. 2 MAPPING BETWEEN LOCAL AND GLOBAL SYSTEMS OF EQUATIONS.

The local coefficient matrices are functions of the horizontal wavenumber  $s$  and the depth  $z$  of the actual interface. As can be observed from Eqs. 16 to 20, the dependence on  $z$  is present only in the exponential function; thus the two local matrices for layer number  $\ell$  can be written as

$$[c]_{\ell}^{\ell-1} = [d]_{\ell} [e]_{\ell}^{\ell-1} \quad (\text{Eq. 35})$$

$$[c]_{\ell}^{\ell} = [d]_{\ell} [e]_{\ell}^{\ell} \quad , \quad (\text{Eq. 36})$$

where  $[d]_{\ell}$  is a matrix that is a function of the horizontal wavenumber only, and  $[e]_{\ell}^i$  is a diagonal matrix containing the exponential functions for interface number  $i$  evaluated in layer number  $\ell$ . By introducing a local coordinate system where the plane  $z=0$  coincides with one of the interfaces, the number of necessary calculations of the complex exponential function can be reduced. If, for example, the interface above the layer is chosen, Eqs. 35 and 36 take the simpler forms:

$$[c]_{\ell}^{\ell-1} = [d]_{\ell} \quad (\text{Eq. 37})$$

$$[c]_{\ell}^{\ell} = [d]_{\ell} [e]_{\ell}^{\ell} \quad . \quad (\text{Eq. 38})$$

To build the global coefficient matrix by means of the pointers defined by Eq. 33, it is necessary only to calculate for each layer the elements of the matrix  $[d]_{\ell}$ , which are very simple functions of the horizontal wavenumber, and the exponentials in  $[e]_{\ell}^{\ell}$ .

Although, from a theoretical point of view, the origin of the local coordinate system can be chosen arbitrarily, its choice is quite important for the numerical stability when large real arguments of the exponential functions appear. This is so for thick layers and large values of the horizontal wavenumber. In these cases a numerical solution based on the original Thomson-Haskell technique becomes unstable, as is clear from the physical significance of the exponential functions. These express the depth behaviour of the field, and when the arguments are imaginary they correspond to up and downgoing conical waves. However, when the arguments become real, as is the case for large horizontal wavenumbers, the waves are inhomogeneous conical waves travelling in the horizontal direction with an exponential decay away from the interfaces (provided that no sources are present in the layer). When the arguments become very large, the field produced at the opposite interface by these exponential "tails" will vanish. At these wavenumbers a thick layer will therefore behave exactly as an infinite halfspace. As the Thomson-Haskell technique requires that the solution is "propagated" through all layers, numerical stability problems obviously



arise because this is impossible at these wavenumbers. By factorizing out the exponential functions a stable solution can be obtained, and several computational schemes for this have been proposed, see for instance Franssens <8>. These modifications of the original technique, however, yield a more complex and time-consuming computer code.

With the present technique it is possible to obtain unconditionally stable solutions by applying gaussian elimination with partial pivoting to Eq. 32 and by choosing proper origins of the local coordinate systems together with a proper mapping. This is demonstrated in detail in Appendix A.

The fact that no special numerical effort, except the pivoting, is needed to ensure numerical stability in this technique is one of the major reasons for the order-of-magnitude improvement in computational speed over that of the modified Thomson-Haskell technique <2>. Another important factor is the mapping technique, which ensures that only a few simple functions of the horizontal wavenumber have to be calculated for each layer. Due to the special band structure of the global coefficient matrix (Fig. 2), gaussian elimination with partial pivoting can be performed very efficiently.

An important advantage of the present technique is that most operations can be easily vectorized, making it very well suited for implementation on an array processor. Because the local coefficient matrices, Eqs. 37 and 38, are similar for all layers, the calculation of the elements, including the square roots and the exponentials, can be vectorized. The indexed move operations of the mapping are carried out very efficiently on array processors, and the gaussian elimination is by nature a sequence of vector operations. The implementation of this technique on an FPS-164 array processor has therefore yielded a considerable improvement in computational speed compared with serial computers, as can be observed from the calculation times given in Sect. 3.

When the system of equations (Eq. 32) has been solved, the kernels in Eqs. 16 to 20 and 23 to 27 can be evaluated at any depth,  $z$ , with the only additional functions needed being  $\exp(\pm z \alpha_n)$ ; all other functions and expressions have been evaluated while setting up the system of equations. The present technique is therefore very efficient if the field is to be determined at many different depths.

It is well known that for guided propagation in loss-less media the kernels in the integral representations will have poles on the real axis corresponding to normal modes, Rayleigh waves, etc. In these cases a direct numerical integration along the real axis is inconvenient. There are two ways in which this problem can be overcome. One is to deform the contour of integration into the complex plane; the other is to introduce physically realistic attenuations in the layers, which will result in the poles moving out into the complex plane and consequently make real-axis integration possible. The latter approach has the advantage that the integration can be performed by means of the Fast Field Technique <1>, and this is the choice made here. It should be stressed however that the solution technique described here is valid for both complex or real values of the horizontal wavenumber 's', and that any complex integration contour could be chosen.

The Bessel functions are expressed in terms of Hankel functions as

$$J_{\ell}(rs) = \frac{1}{2} [H_{\ell}^{(1)}(rs) + H_{\ell}^{(2)}(rs)] \quad (\text{Eq. 39})$$

and each integral is split into two. As only outgoing waves are considered, the integrals involving  $H_{\ell}^{(1)}(rs)$  are neglected, and  $H_{\ell}^{(2)}(rs)$  is replaced by its asymptotic form

$$H_{\ell}^{(2)}(rs) \underset{rs \rightarrow \infty}{\sim} \sqrt{\frac{2}{\pi rs}} e^{-i[rs - (\ell + \frac{1}{2})\frac{\pi}{2}]} \quad (\text{Eq. 40})$$

As shown in <3> this approximation yields insignificant errors for ranges beyond a few wavelengths.

The field integrals now take the form

$$F(r, z) = \frac{1}{\sqrt{2\pi r}} e^{i(\ell + \frac{1}{2})\frac{\pi}{2}} \int_0^{\infty} f(s, z) \cdot \sqrt{s} e^{-irs} ds, \quad (\text{Eq. 41})$$

where  $\ell=0$  for  $w$  and  $\sigma_{zz}$  and  $\ell=1$  for  $u$  and  $\sigma_{rz}$ . The integral in Eq. 41 can be evaluated by means of an FFT, but in order to do this, the interval of integration must be finite. However, because of the exponential decay of the kernels for  $s$  going towards infinity, the truncation error can be made arbitrarily small. The truncated wavenumber space is discretized as follows

$$s_n = s_0 + n\Delta s, \quad n = 0, 1, \dots (M-1). \quad (\text{Eq. 42})$$

In addition, the range interval of interest is discretized as:

$$r_m = r_0 + m\Delta r, \quad m = 0, 1, \dots (M-1), \quad (\text{Eq. 43})$$

where

$$\Delta r \Delta s = \frac{2\pi}{M} \quad (\text{Eq. 44})$$

and  $M$  is a power of 2. The field integrals are now evaluated as

$$F(r_m, z) = \frac{\Delta s}{\sqrt{2\pi r_m}} e^{-i[s_0 r_m - (\ell + 1/2)\pi/2]} \times \sum_{n=0}^{M-1} [f(s_n, z) e^{-ir_0 n \Delta s} \sqrt{s_n}] e^{-i2\pi mn/M}, \quad (\text{Eq. 45})$$

where the summation is performed by means of an FFT yielding the field at all  $M$  ranges, Eq. 43, simultaneously.

In the case of plane geometry the approximation given by Eq. 40 is not needed, and the FFT integration can be performed directly <6>.

### 3 COMPUTATIONAL EXAMPLES

In this section we present numerical solutions to three important propagation problems in underwater acoustics: 1) the Lloyd-mirror interference effect at the sea surface, 2) low-frequency propagation in a shallow-water duct, and 3) reflection of a narrow beam of sound at the sea floor. These problems have been selected so as to demonstrate the full capability of the numerical model described earlier, i.e. its applicability to a wide range of guided and non-guided propagation problems in both plane and cylindrical geometry. The computational efficiency of the code will become apparent from the quoted calculation times on both a VAX-11/750 and on a FPS-164 array processor.

#### 3.1 Sea-surface interference effects

This is a classical problem dealt with in most text books on underwater acoustics <9>. We consider an omnidirectional line source in a halfspace limited above by a perfectly reflecting boundary. The acoustic field in the halfspace (Fig. 3a) becomes quite complex, exhibiting a series of interference beams radiating out at different angles (in the contour plot black indicates high sound intensity and white low sound intensity). A closed-form solution to this problem can be easily derived <9>, showing that the beam pattern arises as an interference effect between the two possible sound paths from source to receiver, namely the direct path and the surface-reflected path. This interference pattern is often referred to as Lloyd-mirror beams, with the beam directions far from the source given by

$$\sin \theta_m = (2m-1) \lambda / 4z_s \quad ,$$

where  $\lambda$  is the acoustic wavelength and  $z_s$  the source depth;  $\theta_m$  is the beam angle relative to horizontal.

The numerical solution given in Fig. 3a is in plane geometry with a line source placed 33.75 m below the sea surface. The frequency is 100 Hz and the water sound speed is 1500 m/s. The source depth is  $2.25 \lambda$ , leading to five Lloyd-mirror beams at angles given by  $\sin \theta_m = (2m-1)/9$  or  $\theta_m = 6.4, 19.5, 33.7, 51.1, \text{ and } 90.0^\circ$ . The computed angular spectrum for this propagation problem is shown in Fig. 3b, and we see that energy is in fact propagating in the directions given by the simple formula, and that the peak intensity is the same in all five beams. The beamwidth, however, increases with increasing beam angle.

The iso-intensity contour plot of Fig. 3a is an exact numerical solution to the sea-surface reflection problem. For a spatial grid of  $50 \times 1024$  points the computation time was 5 min on the VAX-11/750 and 18 s on the FPS-164.

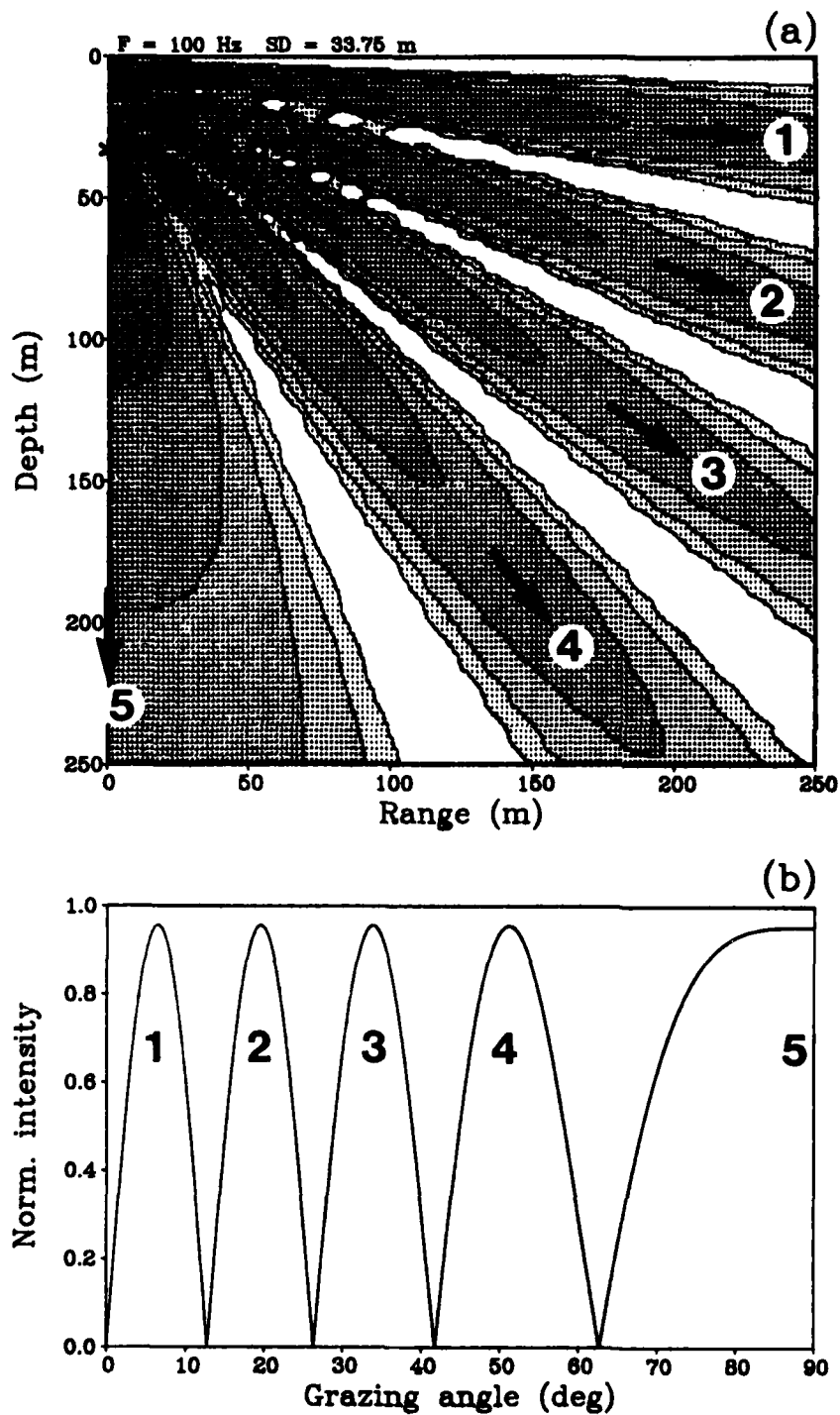


FIG. 3 LLOYD-MIRROR BEAMS AT THE SEA SURFACE (a), AND ASSOCIATED ANGULAR SPECTRUM (b).

Even though the field solution here is available in closed form, many of the standard wave-theory models in ocean acoustics are unable to handle this particular problem. This is so for all normal-mode models that do not include the branch-line integral (continuous spectrum) contribution to the field solution. It is also so for all parabolic equation models, with their inherent small-angle approximation limiting the solution validity to at best  $\pm 40^\circ$  away from the horizontal. This would here mean that only the first three Lloyd-mirror beams would be correctly resolved with the parabolic equation. In fact we consider this particular test problem extremely well-suited for checking parabolic equation solutions, since inherent amplitude and phase errors affect both beam directions and beam intensities.

### 3.2 Propagation in a shallow-water duct

An isovelocity shallow-water duct that is limited above by the sea surface and below by a homogeneous penetrable bottom constitutes a waveguide with interesting frequency-dependent propagation characteristics. We will solve this problem in cylindrical geometry, with environmental parameters as follows: 100 m water depth with a speed of 1500 m/s, a solid bottom with compressional speed of 1800 m/s, shear speed of 600 m/s, compressional attenuation of 0.1 dB/ $\lambda$ , and shear attenuation of 0.2 dB/ $\lambda$ . The density ratio between bottom and water is 2.0. We have intentionally used a solid bottom in order to demonstrate that the often-neglected shear properties can be of considerable importance in low-frequency ocean acoustics.

A full-spectrum solution at 30 Hz is displayed in Fig. 4 for a source at 95 m and a receiver at 100 m (on the bottom). The propagating energy versus horizontal wavenumber is shown on the integrand plot of Fig. 4a, which displays the kernel of Eq. 12 with source contributions included. We have here identified three spectral regions, defined in terms of the phase velocities as:

Evanescent spectrum:  $0 < c_{ph} < 1500$  m/s

Discrete spectrum :  $1500 < c_{ph} < 1800$  m/s

Continuous spectrum:  $1800 < c_{ph}$  ,

where the phase velocity  $c_{ph}$  is related to the horizontal wavenumber 's' through  $c_{ph} = \omega/s$ , with  $\omega$  being the angular frequency of the source. In terms of an angular spectrum the evanescent waves (modes) have non-real angles at the receiver depth. The discrete modes, on the other hand, correspond to propagation angles between horizontal ( $c_{ph}=1500$  m/s) and  $33.6^\circ$  ( $c_{ph}=1800$  m/s), while the continuous modes correspond to steep propagation angles above  $33.6^\circ$ . Thus it is the compressional wave speeds in water and bottom that determine the spectral regions.

We see from the integrand (Fig. 4a) that there are five peaks in the spectrum corresponding to five preferred modes of propagation. There are two discrete modes, two continuous (virtual) modes, and one evanescent

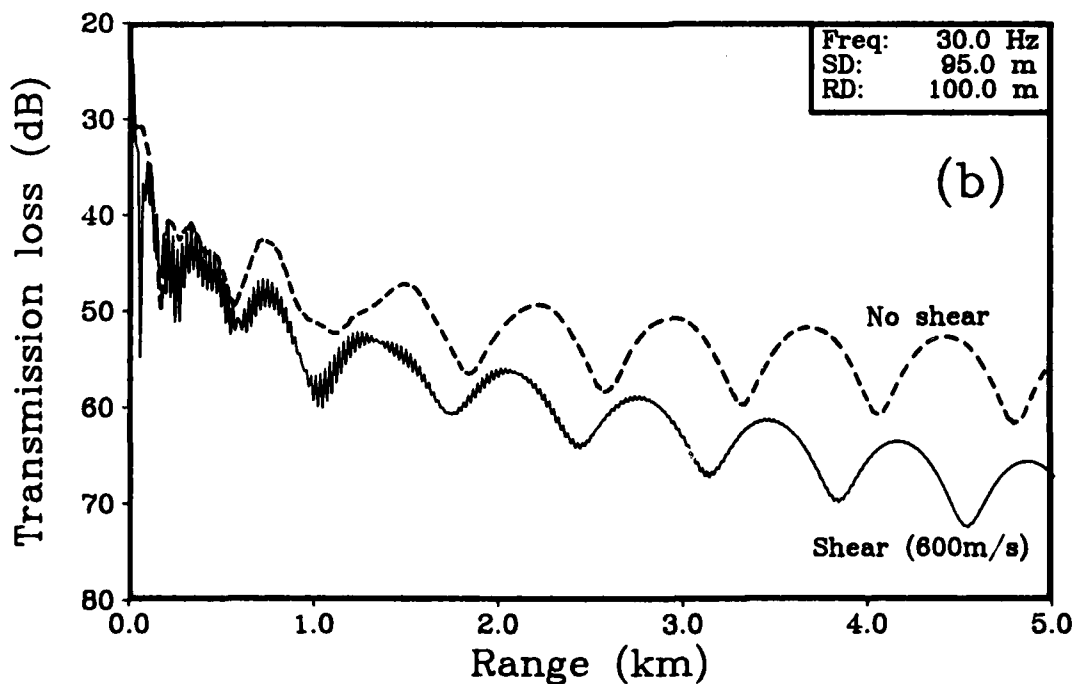
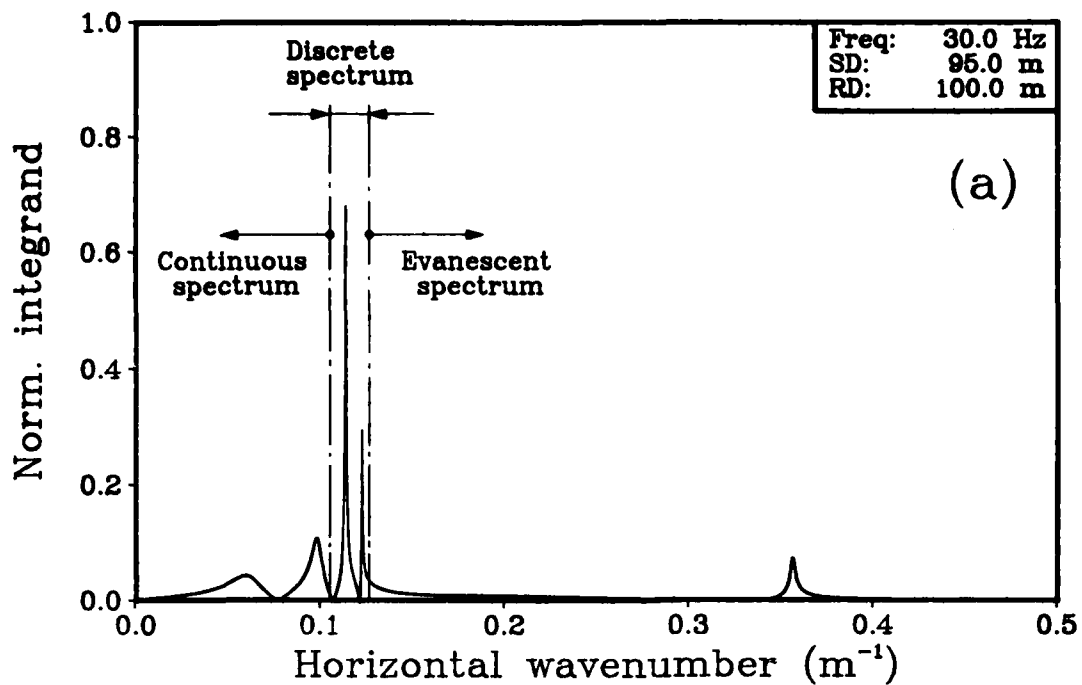


FIG. 4 HORIZONTAL WAVENUMBER SPECTRUM FOR SHALLOW WATER CASE AT 30 Hz (a), AND ASSOCIATED TRANSMISSION LOSS CURVES (b).

mode, which can be shown to be an interface wave of the Scholte type  $\langle 10, 11, 12 \rangle$  propagating along the sea floor. The interface wave has a phase velocity of 530 m/s, which is slower than any of the body waves of this problem (1500, 1800, 600 m/s). Moreover it has its highest amplitude at the water/bottom interface, with exponentially decaying amplitude away from the interface. The existence of the interface wave is intrinsically related to the shear properties of the bottom, and, hence, if we neglect shear we automatically exclude this propagation path.

The integrand plot (Fig. 4a) shows that the two discrete modes have highest excitation and lowest loss (poles located close to the real axis in the complex wavenumber space). The discrete modes will therefore dominate propagation beyond the nearfield, as shown in the lower transmission-loss curve (shear = 600 m/s) of Fig. 4b. Beyond 2 km we have a typical 2-mode interference pattern caused by the discrete modes. The two highly attenuated virtual modes are responsible for the irregularities of the interference pattern at short ranges, while the interface mode causes the "high-frequency" noise on the propagation-loss curve. The above detailed analysis of the contributions of the various spectral components to the propagation-loss curve can be demonstrated explicitly by solving for just selected parts of the wavenumber spectrum.

A full-spectrum calculation without shear shows better propagation at long ranges, but with essentially the same interference structure (Fig. 4b). Hence the effect of shear is here to increase losses for waterborne propagation.

We now move to a frequency of 5 Hz (Fig. 5), which is below the cut-off frequency for discrete modes. Here the effect of shear is to make propagation conditions better than they are in the case where shear is neglected (see Fig. 5b). Let us shortly analyze the spectral content of the integrand plot (Fig. 5a). There are no discrete modes and only one highly damped virtual mode. The important peak, however, is associated with the interface wave, which has low attenuation and therefore becomes the most important propagation path at this frequency. The resulting propagation loss (Fig. 5b), with a shear speed of 600 m/s, shows interference between the virtual mode and the interface mode. However, since the virtual mode is highly attenuated, only the interface mode remains at long ranges (beyond 5 km). If we neglect shear there is no interface mode; propagation thus becomes very poor because energy can then propagate only in the continuous mode. On the other hand, we notice from Figs. 4 and 5 that when shear is included, propagation is just as good at 5 Hz as it is at 30 Hz, even though the propagation mechanisms are quite different in the two cases. The importance of shear in low-frequency ocean acoustics has been addressed in more detail elsewhere  $\langle 10, 11 \rangle$ .

The numerical model described in this paper is extremely well suited for solving low-frequency guided wave-propagation problems. A full-spectrum solution is readily available with minimum computational effort. A propagation-loss curve, such as shown in Fig. 4 or 5, is produced in 65 s on the VAX-11/750 and in just 5 s on the FPS-164. These computation times relate to the use of 2048 integration points along the wavenumber axis.

The most commonly used models for solving guided propagation problems are

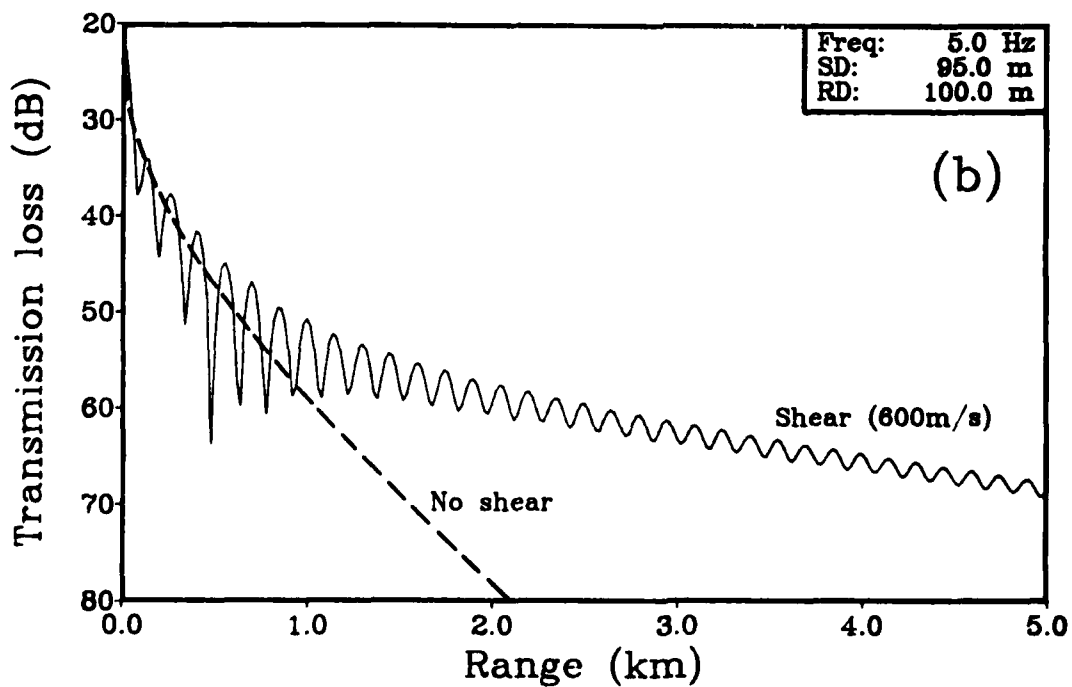
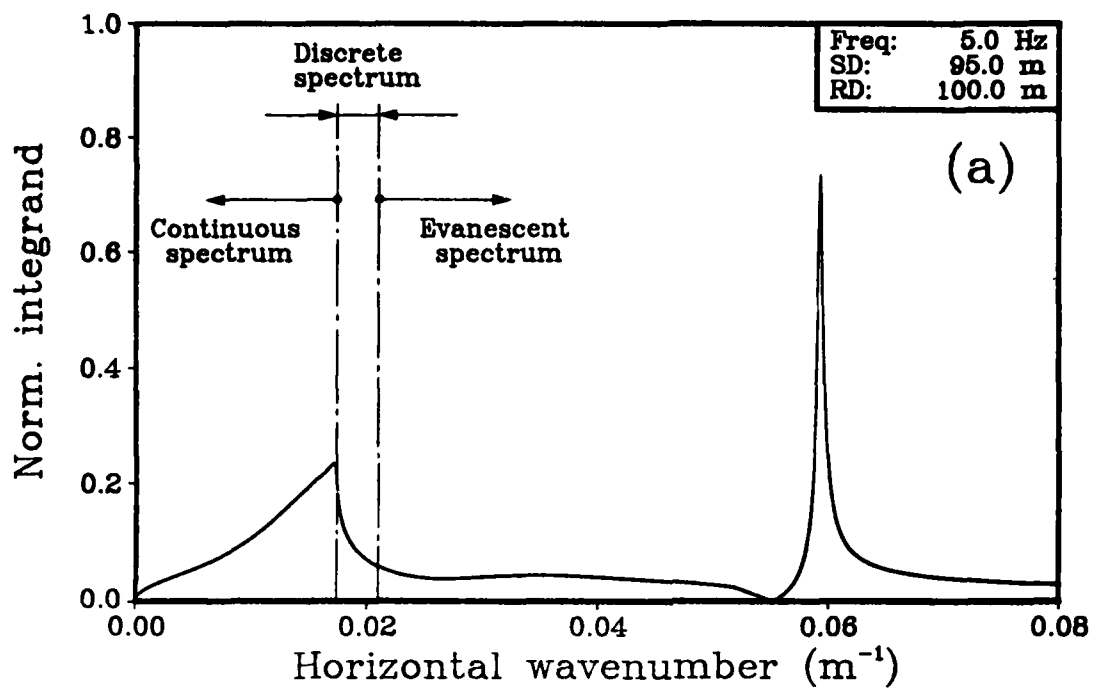


FIG. 5 HORIZONTAL WAVENUMBER SPECTRUM FOR SHALLOW WATER CASE AT 5 Hz (a), AND ASSOCIATED TRANSMISSION LOSS CURVES (b).



based on normal-mode theory. Again, if such a model does not include the branch-line integral, the continuous spectrum is not included. Moreover, most normal-mode models solve a real eigenvalue problem, and hence neglect shear altogether, or at best include shear in a perturbational manner as just a loss mechanism. In any event, the interface wave is not part of the modal solution, and hence such a model would fail when applied to a propagation problem not dominated by discrete modes.

The full-spectrum solution technique presented here is clearly superior to most existing models in handling guided-wave propagation in horizontally stratified fluid/solid layers. Only in the case of many guided low-loss modes do numerical problems arise, since many integration points are then needed in order to resolve the peaks in the integrand.

### 3.3 Beam reflection at a water/bottom interface

In this last example we study the reflection and transmission of a narrow beam of sound at a water/bottom interface. This example has been chosen to demonstrate that directional sources (beams) are handled by the numerical model in a computationally efficient manner. The beam is generated by a vertical source array composed of a number of equidistantly spaced line sources (plane geometry), and the resulting acoustic field is found by superposition of the contributions from the individual sources, as described in Sect. 1. The beam direction is varied by appropriately phasing the source elements, and the intensity distribution across the beam can be selected by applying an amplitude weighting across the array. By varying the array distance from the interface and the number of source elements (half-wavelength spacing), a beam of arbitrary width can be generated. Moreover, beams can be focused or defocused by phasing the sources appropriately. By using a "physical" array of finite length to generate the beam we automatically ensure that only realistic beams are generated, i.e. a focused beam in water (with realistic attenuation) cannot be infinitely narrow, because that would lead to infinite intensity in the focal plane, which is unphysical. Hence this model treats an entirely realistic physical system.

The interest in the beam-reflection problem goes back to an experimental study by Muir et al <13>, where it was shown in a laboratory experiment that a narrow beam of sound impinging on the bottom at grazing angles below the critical angle will not be totally reflected as predicted for an infinitely wide plane wave. Instead there is significant energy transmitted into the bottom, this energy increasing as the incident beam narrows. This interesting observation has remained unexplained for years, but we shall demonstrate numerically that the beam penetration is a simple consequence of the angular spectrum shape associated with narrow beams.

The beam reflection/transmission problem will be solved in plane geometry for an environment similar to the one used by Muir et al <13>. We consider a water halfspace overlying a fluid-bottom halfspace. The sound speeds are 1450 m/s in the water and 1675 m/s in the bottom, giving a critical (grazing) angle of exactly  $30^\circ$ . The density ratio between bottom and water is 2.0 and we initially neglect attenuation in the bottom. Calculations are done for a frequency of 20 kHz, which gives an acoustic wavelength ( $\lambda$ )

in the water of 7.25 cm. We have chosen a source array of 121 elements with  $\lambda/2$  spacing, giving an array length of 4.25 m. A gaussian amplitude weighting was applied across the array, producing a gaussian beam with low sidelobe levels.

Calculated field solutions are given in Fig. 6 for a focused beam that is  $2.5\lambda$  wide at the interface. The beamwidth is measured across the beam between the 3-dB down points. The arrows in the upper part of Fig. 6 indicate the beam directions; also shown are the angles of incidence ( $\theta_i$ ), reflection ( $\theta_r$ ), and transmission ( $\theta_t$ ), all measured along the direction of maximum amplitude in a beam with respect to horizontal. Three cases are considered,  $\theta_i = 25.0^\circ, 30.0^\circ, 35.0^\circ$ , with the critical angle being  $30^\circ$ . Hence the upper beam is incident at  $5^\circ$  below the critical angle, and a transmitted beam is still present in the bottom ( $\theta_t = 11.5^\circ$ ). With increasing angle of incidence more energy is propagated into the bottom (contours show losses in arbitrary dB's). We also notice that the angle of reflection is lower than the angle of incidence (non-specular reflection). These beam reflection and transmission properties are in qualitative agreement with the experimental results reported by Muir et al <13>, even though the experiment was carried out with a true 3-dimensional pencil beam, while the calculations here are done for a 2-dimensional beam.

A full understanding of the observed beam behaviour can be obtained by comparing the spectral content of the incident beam with the angular reflectivity characteristics of the interface, as shown in Fig. 7. The upper figure displays angular spectra for beams of different widths and incident at the critical angle. Note that the narrow beam has the widest spectrum, while the spectral width decreases with increasing beamwidth. In this angular representation an infinitely wide plane wave becomes a delta function with only one direction of propagation. Any beam of finite width has a spectrum of finite width; the very narrow beams have broad spectra, indicating that energy is propagating over a wide range of angles. Hence it is a contradiction to state that narrow beams are highly directional <13,14>.

Let us concentrate on the wide spectrum in Fig. 7a ( $D = 2.5\lambda$ ), which has its peak energy propagating at  $30^\circ$  but also has significant energy propagating at  $20^\circ$  and  $40^\circ$ . Hence many propagation directions are associated with the narrow beam. Figure 7b shows the plane-wave reflection loss and phase shift versus angle at the interface, indicating perfect reflection below  $30^\circ$  with a phase shift, and an increasing reflection loss above  $30^\circ$  with no phase shift. Comparing Figs. 7a and 7b shows that the left (hatched) half of the beam spectra are perfectly reflected (though with a phase shift) while the right half is partly transmitted. Thus in practice we need to weight the incident-beam spectrum with the reflectivity characteristics of the interface in order to get the spectrum for the reflected or transmitted beam. The above simple argument explains qualitatively what to expect. For example, the hatched part of the spectrum will be entirely reflected, while the right half will be partly transmitted. The different weightings put on the two half-spectra mean that the peak energy in the reflected beam moves to smaller angles ( $\theta_r < \theta_i$ ), as also observed in Fig. 4. On the other hand, only energy in the right half of the spectrum will be transmitted, and the beam direction ( $\theta_t$ ) can be determined from the peak in the transmitted spectrum.

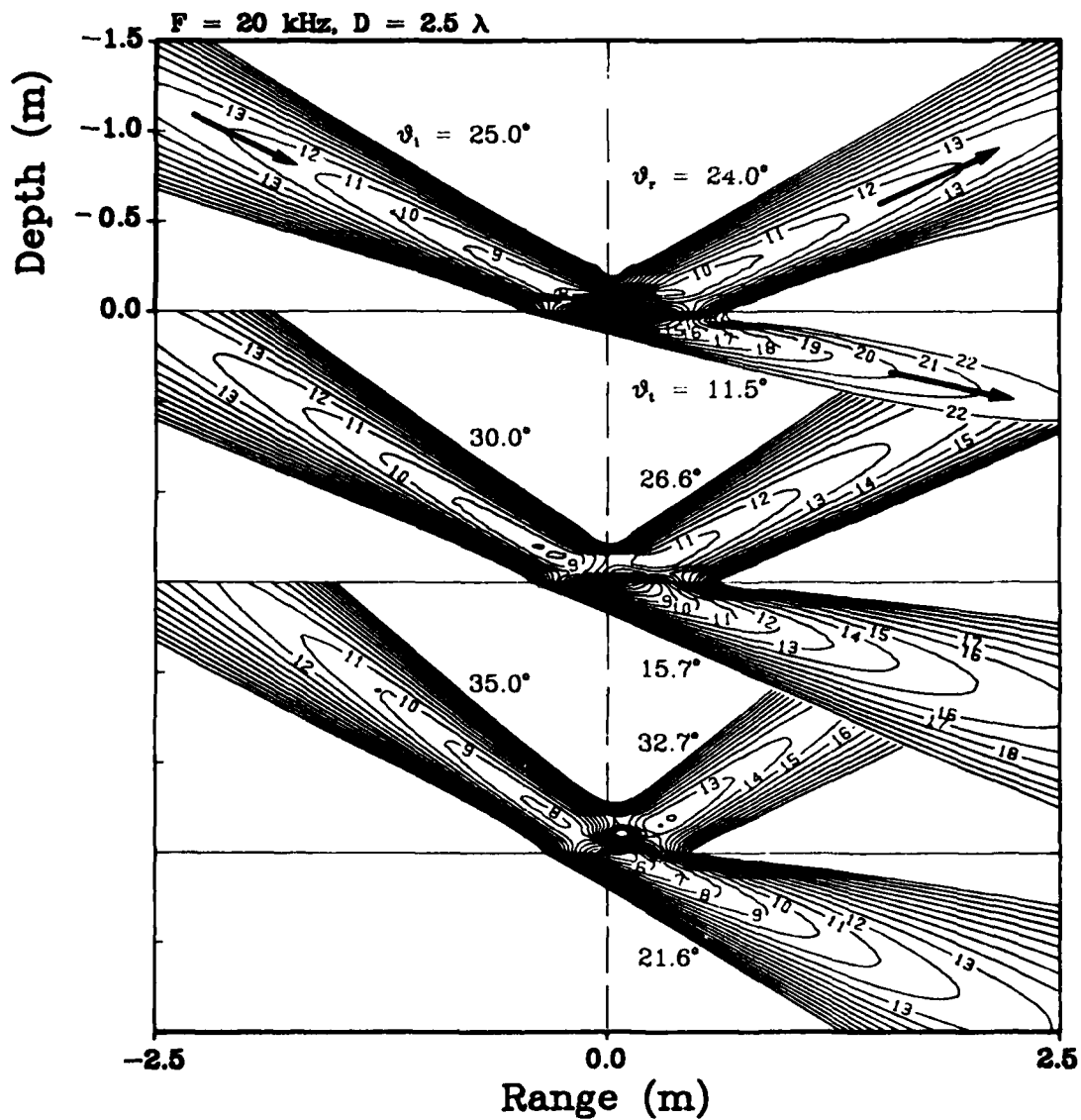


FIG. 6 REFLECTION AND TRANSMISSION OF NARROW BEAM OF SOUND ( $D=2.5\lambda$ ) AT WATER/BOTTOM INTERFACE. THE CRITICAL ANGLE IS  $30^\circ$  AND THERE IS NO ATTENUATION IN THE BOTTOM.

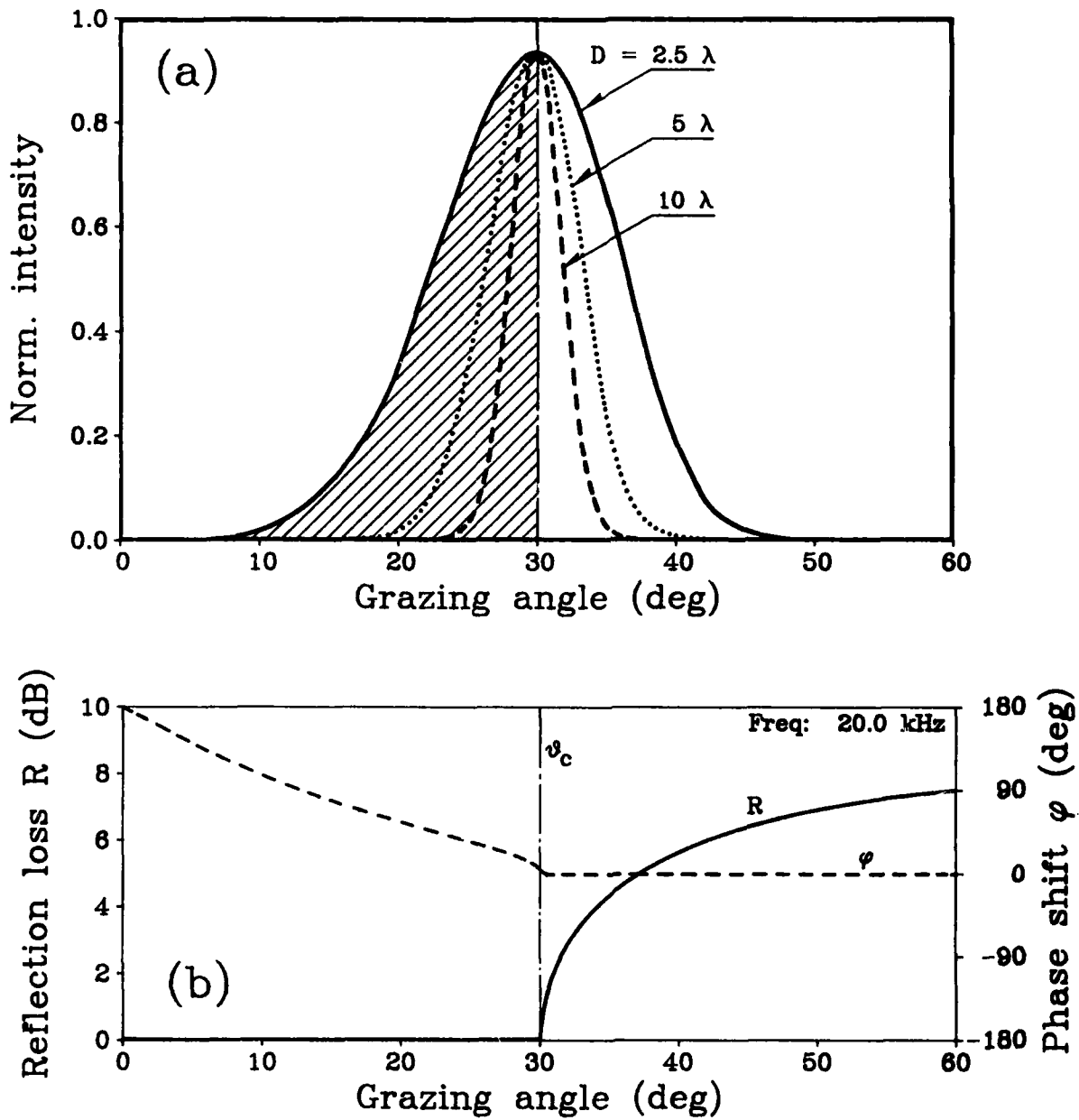


FIG. 7 ANGULAR SPECTRA OF INCIDENT BEAMS OF DIFFERENT HALF-POWER WIDTHS (a), AND REFLECTIVITY CHARACTERISTICS AT WATER/BOTTOM INTERFACE (b).

It is clear from Fig. 7 that even though each spectral component is reflected and transmitted according to Snell's law, the total beam, in which phase and amplitude weightings are applied to the broad spectrum, cannot be expected to be so. On the other hand, the beam results should approach Snell's law for increasing beamwidth (decreasing spectral width). In fact, as shown in Fig. 8, we do retrieve Snell's law in the limit of very wide beams.

Finally, when a realistic bottom loss of  $0.8 \text{ dB}/\lambda$  is included we notice no substantial effect on the calculated beam angles, even though the transmitted beam becomes strongly attenuated.

One last point will be briefly addressed. It was noted in the experimental results <13> that the transmitted beam was horizontally displaced, i.e. the incident and transmitted beam axes intersect the interface at different points. A closer look at Fig. 6 shows that both the reflected and the transmitted beam centres are displaced; this is because a lateral wave is excited when energy is incident on the interface below the critical angle. The reflected and transmitted fields are then composed of contributions from both the "specular" beam and the lateral wave field, causing an apparent lateral displacement of the beams. The displacement can be both forward and backward and will be a function of beamwidth as well as of angle of incidence. Furthermore, reflected and transmitted beams will generally have different displacements.

The computational efficiency of the numerical code is particularly evident for this case, in which field calculations from 121 sources have been made on a spatial grid of  $50 \times 512$  points. Each contoured beam plot in Fig. 6 takes 6 min on the VAX-11/750 and 21 s on the FPS-164. Not only are these acceptable calculation times, but this code seems to be the only one capable of doing these types of calculations.

The results presented here are exact numerical solutions for 2-dimensional beams, against which approximate solutions <14> can be checked. Similar beam reflection studies at fluid/solid interfaces have been reported by the authors elsewhere <6,15,16>.

#### SUMMARY AND CONCLUSIONS

We have presented an efficient numerical solution technique for general applications to wave propagation in horizontally stratified viscoelastic media. The model provides a full-wave solution for the field generated by a single source as well as for that generated by a vertical source array. It allows the spatial distribution of the acoustic field to be evaluated at least one order of magnitude faster than with existing models based on the Thomson-Haskell solution technique. The computational examples clearly demonstrate the model's versatility in providing exact solutions to a wide range of guided and non-guided propagation problems in underwater acoustics, but the model is equally applicable to problems in ultrasonics and seismics. Moreover, the computational efficiency of the numerical code has made it feasible (on array processors) to perform pulse calculations based on Fourier synthesis of time signals, even when hundreds of frequency samples are needed.

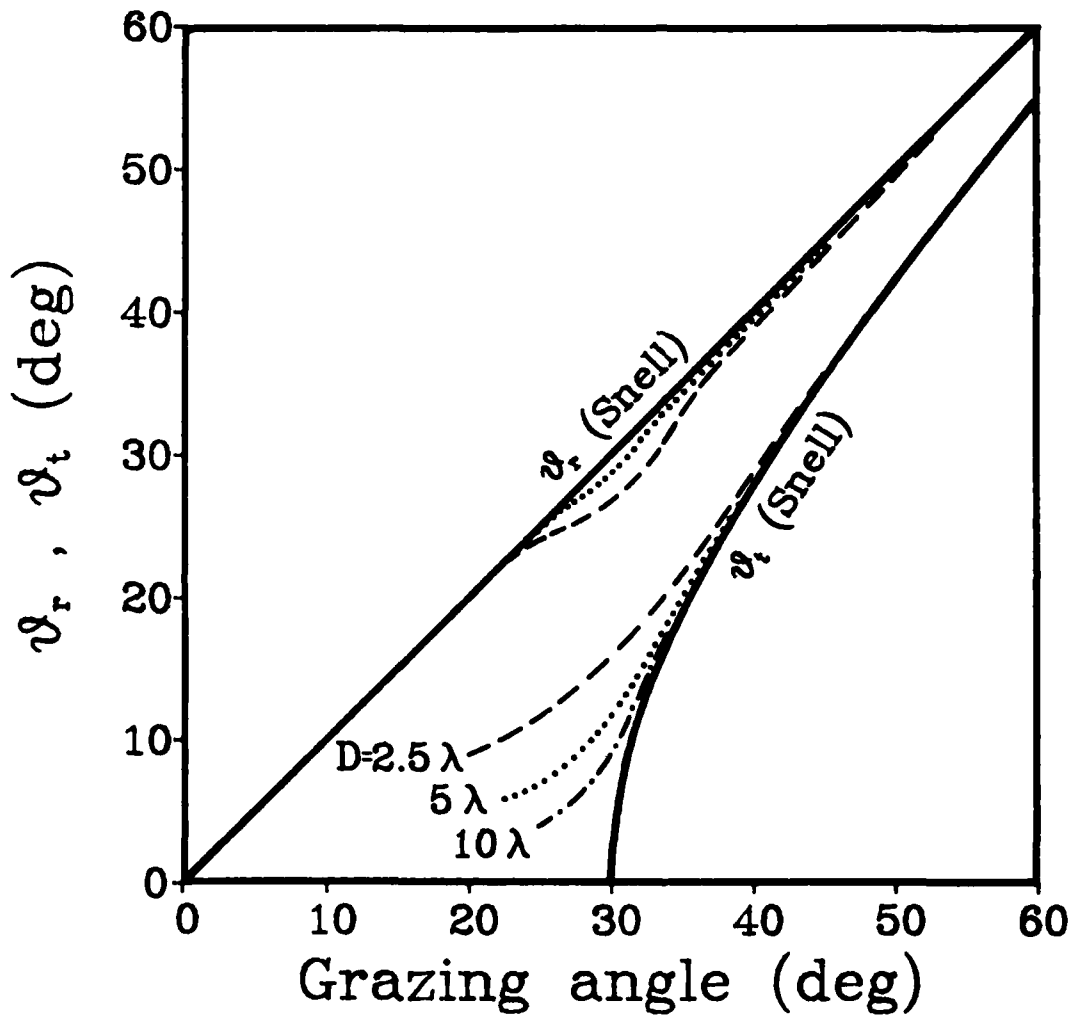


FIG. 8 DEVIATION FROM SNELL'S LAW FOR REFLECTION AND TRANSMISSION OF NARROW BEAM OF SOUND AT WATER/BOTTOM INTERFACE. Bottom attenuation is neglected and the indicated beamwidths are measured between the 3 dB down points of the incident beam at the interface.

## APPENDIX A

### NUMERICAL STABILITY

The physically realistic attenuation introduced in the environment makes the global system of equations (Eq. 32) theoretically well conditioned for real horizontal wavenumbers. Because of the limited accuracy of digital computers, this does not, however, guarantee stability of the numerical solution technique. In this paper gaussian elimination is used to solve Eq. 32, which, in general, requires scaling and pivoting to ensure numerical stability.

Equations 16 to 20 of the main text show that the difference in dimension between the displacements and the stresses can yield several orders of magnitude in difference between the coefficients in the corresponding Eqs. 29 and 32. In such cases gaussian elimination with partial pivoting will not ensure unconditional stability, owing to truncation errors. The equations therefore have to be scaled in order to make all coefficients dimensionless. The choice of actual scaling factors is not critical. Here all stress equations are divided by the constant  $\omega^2 \rho_s$ , where  $\rho_s$  is the density of any layer. The displacement equations are made dimensionless by dividing by the wavenumber  $h_s$  for the same layer.

For purely imaginary arguments of the exponential functions, the magnitude of the exponentials is unity, and the solution will be unconditionally stable. For real arguments, i.e. the evanescent regime with  $s > h_n$  or  $k_n$ , large differences in order of magnitude can however appear again. In this case the differences appear within the rows, and scaling of rows is therefore not applicable. Scaling of columns could theoretically be applied, but this requires considerable additional computations at each horizontal wavenumber, and the problem of exponential overflow in the actual computer would still remain. With a little help from the physical significance of the problem it is however straightforward to obtain stability also in this case, without any additional computational effort.

This is most easily demonstrated by means of an example. Consider a series of fluid layers with a very thick layer 'n' below the lowermost source. In the evanescent case, i.e.  $s \gg h_n$ , this layer will behave like an infinite half space, which means that the arbitrary function  $A_n^+$  associated with the

exponentially increasing depth function ( $e^{2\alpha_n}$ ) should vanish. The solution of the global system of equations (Eq. 32) by means of gaussian elimination with partial pivoting can be forced to yield this behaviour automatically simply by choosing a mapping that yields the structure of the system showed in Fig. A1. The upper boundary of the layer, i.e. interface n-1, is selected as the origin of the local coordinate system, which removes the exponentials from the submatrix  $[c]_n^{n-1}$ . When the argument to the exponential functions in  $[c]_n^n$  becomes large it is simply truncated; the column

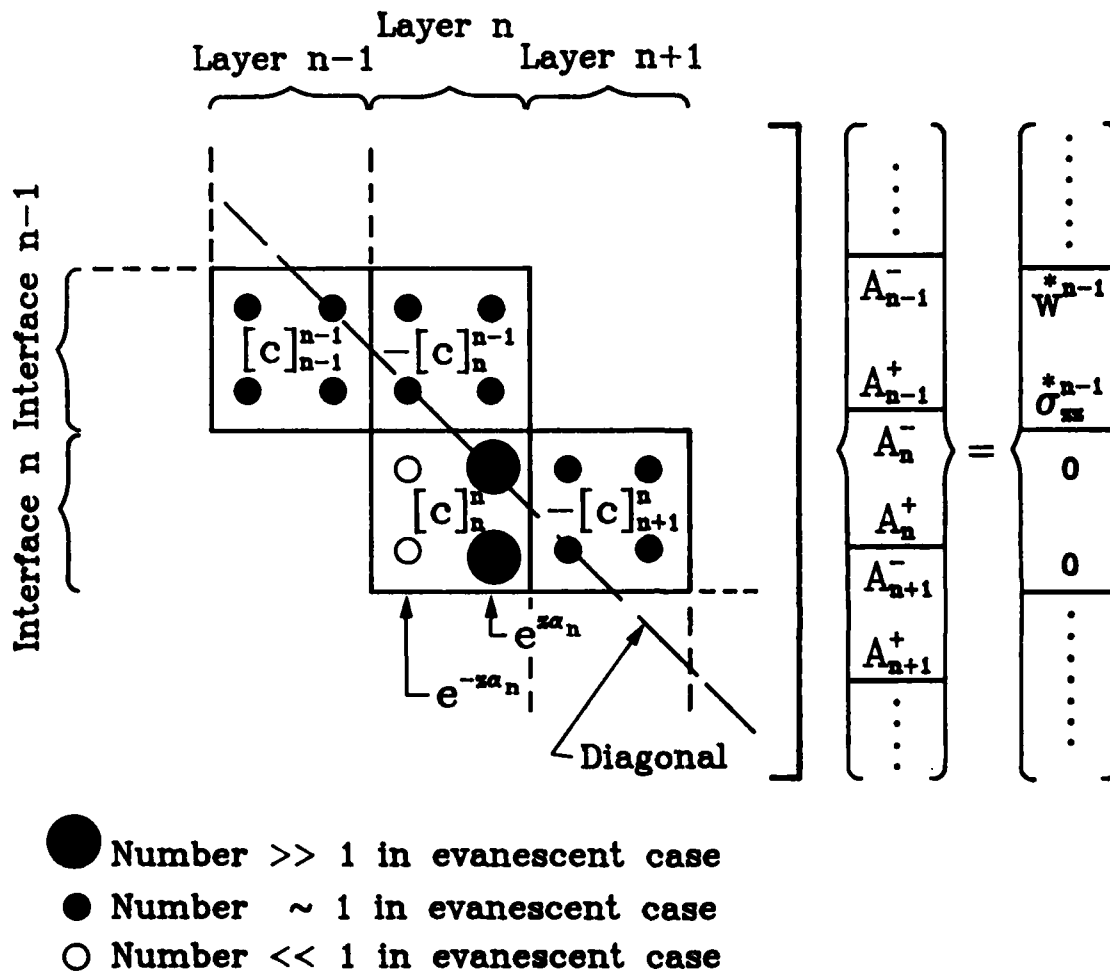


Fig. A.1 MAPPING ENSURING NUMERICAL STABILITY IN EVANESCENT CASE.



closest to the diagonal of the global system then contains at least one very large number, whereas the lefthand column contains two almost vanishing numbers. No pivoting will then be performed between the submatrices  $[c]_n^{n-1}$  and  $[c]_n^n$ . As no sources are present in the layers  $>n$ , the right-hand sides corresponding to interfaces  $>n$  will then always be zero.

The element of  $[c]_n^n$  placed on the diagonal of the global system remains very large (eventually after pivoting with the row below) compared with the other elements in that row and will therefore force the corresponding arbitrary function  $A_n^+$  to be zero after triangulation and back-substitution.

The lowest equation for interface  $n-1$  then yields the correct value of  $A_n^-$ , and back-substitution can continue.

In a similar way it can be shown that for layers above the uppermost source the origin of the local coordinate system must be placed at the lower boundary in order to ensure numerical stability if the columns of the submatrices are organized as shown in Fig. A1. Stability problems can then appear only in two cases. The first is when sources are placed within a very thick layer, but this can be avoided by adding dummy interfaces above and below the sources. The other is the rather unrealistic situation in which sources are present on both sides of a thick layer. The solution of such a problem would require two separated solutions if the evanescent regime is considered.

In the case of solid layers, unconditional stability is ensured in the same way but because two large exponentials can appear in any layer it is slightly more complicated to demonstrate.

#### REFERENCES

1. DINAPOLI, F.R. Fast field program for multilayered media, Report 4103. New London, CT, US Naval Underwater Systems Center, 1971.
2. KUTSCHALE, H.W. Rapid computation by wave theory of propagation loss in the Arctic Ocean, Technical Report CU-8-73. Palisades, NY, Columbia University, Lamont Geological Observatory, 1973.
3. DINAPOLI, F.R. and DEAVENPORT, R.L. Theoretical and numerical Green's function field solution in a plane multilayered medium, Journal of the Acoustical Society of America, 67, 1980: 92-105.
4. KENNETT, B.N.L. Seismic Wave Propagation in Stratified Media. Cambridge U.K., Cambridge University Press, 1983.
5. EWING, W.M., JARDETZKY, W.S. and PRESS, F. Elastic Waves in Layered Media. New York, NY, McGraw-Hill, 1957: ch. 4.
6. SCHMIDT, H. and JENSEN, F.B. A full wave solution for propagation in multilayered viscoelastic media, with application to gaussian beam reflection at fluid/solid interfaces. (Submitted to the Journal of the Acoustical Society of America).

7. REID, J.K. Direct solution of finite element and finite-difference equations. In: GLADWELL, I. and WAIT, R. eds. A Survey of Numerical Methods for Partial Differential Equations, Oxford, Clarendon Press, 1979: ch. 15.
8. FRANSSENS, G.R. Calculation of the elasto-dynamic Green's function in layered media by means of a modified propagator matrix method, Journal of the Royal Astronomical Society, 75, 1983: 669-691.
9. BREKHOVSKIKH, L.M. and LYSANOV, Y. Fundamentals of Ocean Acoustics, Berlin, Springer, 1982: pp. 71.
10. AKAL, T. and JENSEN, F.B. Effects of the sea-bed on acoustic propagation, SM-167. La Spezia, Italy, SACLANT ASW Research Centre, 1983. [AD A137 251].
11. SCHMIDT, H. Numerical modelling of seismic interface waves, SM-169. La Spezia, Italy, SACLANT ASW Research Centre, 1983. [AD A137 250]
12. SCHMALFELDT, B. and RAUCH, D. Explosion-generated seismic interface waves in shallow water: experimental results, SR-71. La Spezia, Italy, SACLANT ASW Research Centre, 1983. [AD A134 551]
13. MUIR, T.G., HORTON, C.W. Sr., and THOMPSON, L.A. The penetration of highly directional acoustic beams into sediments, Journal of Sound and Vibration, 64, 1979: 539-551.
14. TJOTTA, J.N. and TJOTTA, S. Theoretical study of the penetration of highly directional acoustic beams into sediments, Journal of the Acoustical Society of America, 69, 1981: 998-1008.
15. JENSEN, F.B. Numerical models in underwater acoustics, In: FELSEN, L.B. ed. Proceedings of the NATO Advanced Research Workshop on Hybrid Formulation of Wave Propagation and Scattering, Rome, Italy. 30 August - 3 September, 1983. The Hague, Nijhoff, 1984.
16. SCHMIDT, H. Modelling of pulse propagation in layered media using a new fast-field program. In: FELSEN, L.B. ed. Proceedings of the NATO Advanced Research Workshop on Hybrid Formulation of Wave Propagation and Scattering, Rome, Italy. 30 August - 3 September, 1983. The Hague, Nijhoff, 1984.

KEYWORDS

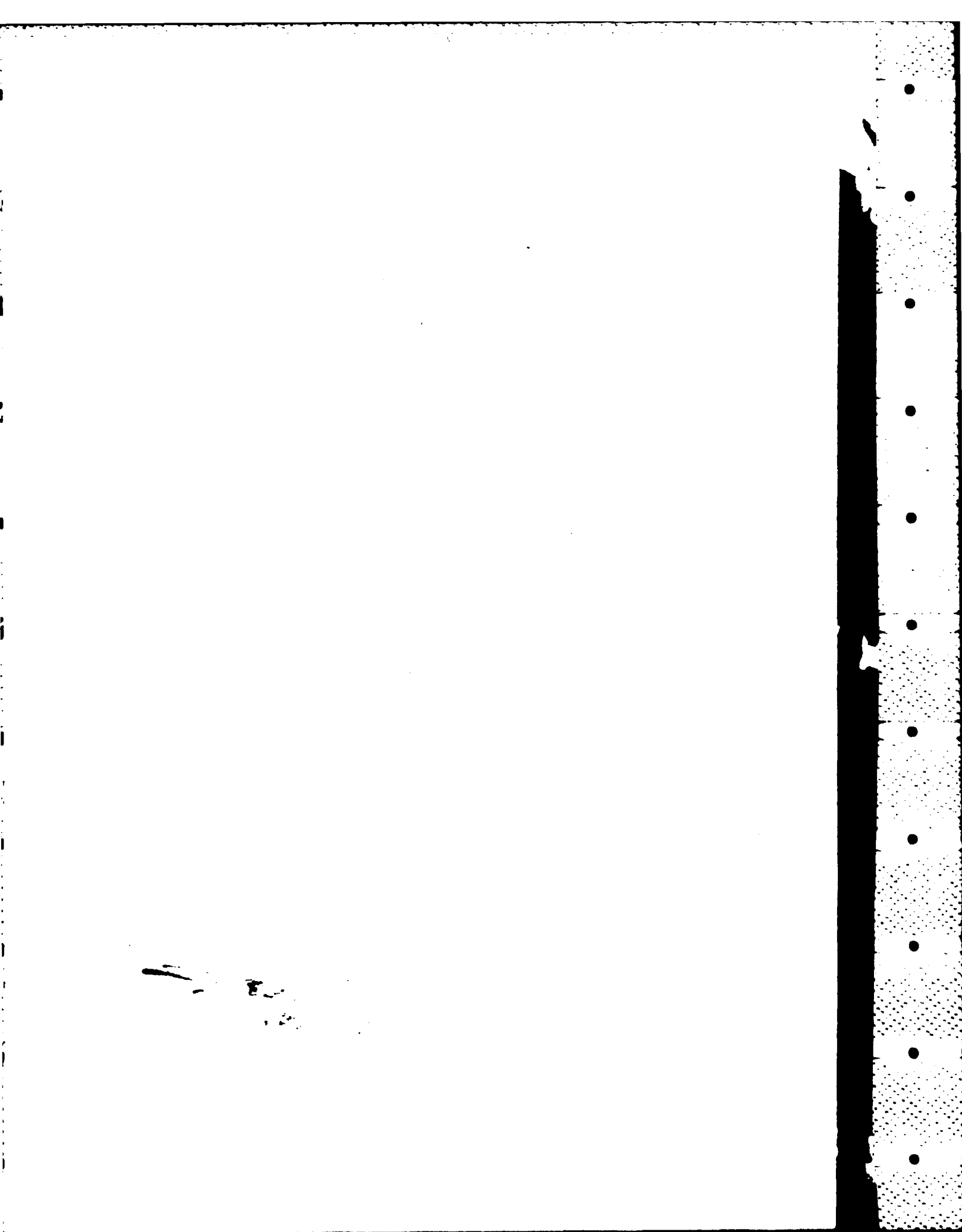
ACOUSTIC FIELD  
ATTENUATION  
BEAM PENETRATION  
BOTTOM REFLECTION  
BOUNDARY CONDITIONS  
COMPRESSIONAL ATTENUATION  
COMPRESSIONAL SPEED  
COMPRESSIONAL WAVE SPEED  
COMPRESSIONAL WAVES  
CONICAL WAVES  
CONTINUOUS SPECTRUM  
DISCRETE SPECTRUM  
EVANESCENT SPECTRUM  
EVANESCENT WAVES  
FAST FIELD PROGRAMS  
FOURIER SYNTHESIS  
FULL WAVE FIELD RESPONSE MODELS  
FULL WAVE SOLUTION  
GAUSSIAN ELIMINATION  
GLOBAL COEFFICIENT MATRIX  
GRAZING ANGLES  
GUIDED PROPAGATION  
HANKEL TRANSFORM  
HOMOGENEOUS VISCOELASTIC CONTINUA  
HOMOGENEOUS WAVE EQUATION  
HOOKE'S LAW  
HORIZONTAL STRATIFICATION  
HORIZONTAL WAVENUMBER  
INTEGRAL TRANSFORMS  
INTERFACE WAVE  
INTERFACE  
ISOTROPIC VISCOELASTIC CONTINUA  
LLOYD MIRROR INTERFERENCE EFFECTS  
LOW FREQUENCY GUIDED WAVE PROPAGATION  
LOW FREQUENCY PROPAGATION  
MAPPING  
NARROW BEAM  
NON GUIDED PROPAGATION  
PHASE VELOCITY  
PIVOTING  
PLANE WAVE REFLECTION LOSS  
PROPAGATION  
REFLECTION  
SEA FLOOR  
SEA SURFACE INTERFERENCE  
SHALLOW WATER DUCT  
SHEAR ATTENUATION  
SHEAR SPEED  
SHEAR WAVES  
SINGLE SOURCE  
SNELL'S LAW  
SOUND SPEED  
SPATIAL DISTRIBUTION  
THOMSON HASKELL SOLUTION  
TRANSMISSION  
UNDERWATER ACOUSTICS  
VECTORIZATION  
VERTICAL SOURCE ARRAY  
VISCOELASTIC MEDIA  
WAVE EQUATION  
WAVE PROPAGATION

FREQUENCIES

30 Hz  
5 Hz  
20 kHz

INITIAL DISTRIBUTION

	Copies		Copies
<u>MINISTRIES OF DEFENCE</u>		<u>SCNR FOR SACLANTCEN</u>	
JSPHQ Belgium	2	SCNR Belgium	1
DND Canada	10	SCNR Canada	1
CHOD Denmark	8	SCNR Denmark	1
MOD France	8	SCNR Germany	1
MOD Germany	15	SCNR Greece	1
MOD Greece	11	SCNR Italy	1
MOD Italy	10	SCNR Netherlands	1
MOD Netherlands	12	SCNR Norway	1
CHOD Norway	10	SCNR Portugal	1
MOD Portugal	2	SCNR Turkey	1
MOD Spain	2	SCNR U.K.	1
MOD Turkey	5	SCNR U.S.	2
MOD U.K.	20	SEC GEN Rep. SCNR	1
SECDEF U.S.	68	NAMILCOM Rep. SCNR	1
<u>NATO AUTHORITIES</u>		<u>NATIONAL LIAISON OFFICERS</u>	
Defence Planning Committee	3	NLO Canada	1
NAMILCOM	2	NLO Denmark	1
SACLANT	10	NLO Germany	1
SACLANTREPEUR	1	NLO Italy	1
CINCWESTLANT/COMOCEANLANT	1	NLO U.K.	1
COMSTRIKFLTANT	1	NLO U.S.	1
COMIBERLANT	1		
CINCEASTLANT	1	<u>NLR TO SACLANT</u>	
COMSUBACLANT	1	NLR Belgium	1
COMMAIREASTLANT	1	NLR Canada	1
SACEUR	2	NLR Denmark	1
CINC NORTH	1	NLR Germany	1
CINC SOUTH	1	NLR Greece	1
COMNAVSOUTH	1	NLR Italy	1
COMSTRIKFORSOUTH	1	NLR Netherlands	1
COMEDCENT	1	NLR Norway	1
COMMARAIRED	1	NLR Portugal	1
CINCHAN	3	NLR Turkey	1
		NLR UK	1
		NLR US	1
		Total initial distribution	249
		SACLANTCEN Library	10
		Stock	21
		Total number of copies	280



**END**

**FILMED**

**1-85**

**DTIC**